Phenotypic Variability Shapes Bacterial Responses to Opposing Gradients

Lusi Li [1], Xuanqi Zhang,[2,3] Yanhong Sun,[4] Qi Ouyang [1,4] Yuhai Tu,[5,*] and Chunxiong Luo [4,6,†]

[1]*Peking-Tsinghua Center for Life Sciences, Peking University, Beijing 100871, China*
[2]*Department of Systems Biology, Harvard Medical School, Boston, Massachusetts 02115, USA*
[3]*Department of Data Science, Dana-Farber Cancer Institute, Boston, Massachusetts 02215, USA*
[4]*The State Key Laboratory for Artificial Microstructures and Mesoscopic Physics, School of Physics,*
Peking University, Beijing 100871, China
[5]*IBM T. J. Watson Research Center, Yorktown Heights, New York 10598, USA*
[6]*Wenzhou Institute University of Chinese Academy of Sciences, Wenzhou, Zhejiang 325001, China*

Although bacterial chemotaxis behavior in a single gradient has been well studied, chemotaxis of bacterial population in complex environments is not well understood. Here, we discovered four distinct behaviors of *Escherichia coli* populations in microfluidic experiments with different opposing gradients of MeAsp and serine. By using a population chemotaxis model based on the dynamics of intracellular signaling pathways, we found that the nongenetic variability of the relevant chemoreceptors (Tar and Tsr) within the population is responsible for the diverse population behaviors. Through analyses combining the phenotype-to-performance mapping and Tar/Tsr ratio distribution, we predicted the phase diagram of population chemotaxis behaviors under varying chemical gradients and the effect of growth period on population behaviors, which were verified by additional experiments. Our study suggests that phenotypic heterogeneity in chemoreceptors enables diverse chemotactic strategies, which cells may adopt to improve their population fitness in complex environments.

I. INTRODUCTION

The chemotaxis system enables living cells to sense and respond to a variety of environmental stimuli [1–5], which allows cells to move to more favorable locations by ascending chemoattractant (usually nutrients and orienting cues) gradients or descending repellent gradients. As one of the best understood biological systems, the molecular mechanisms of *Escherichia coli* chemotaxis have been elucidated [6–10]. An *E. coli* cell exhibits a run-and-tumble motion with a switching frequency between the two modes of motion (run and tumble) depending on the external chemical stimuli [11]. *E. coli* senses and responds to chemical signals primarily through five transmembrane chemoreceptors: the two major receptors (Tar and Tsr), which together account for 90% of the total number of receptors, and the minor receptors (Tap, Trg, and Aer) [12,13]. The binding of chemoreceptors to chemical ligands inactivates the receptor-CheW-CheA complex, thereby inhibiting the autophosphorylation activity of CheA, which in turn reduces the phosphorylation of the response regulator CheY. A lower level of CheY-P suppresses the tumbling frequency of the bacterial flagellar motor, which increases the run duration

of the cell. The chemosensory system can also adapt to a constant level of stimulus and thus allows *E. coli* cells to climb up attractant gradients and migrate down repellent gradients in a biased run-and-tumble random walk.

While the chemotactic behavior of *E. coli* migrating along a single chemoeffector gradient has been investigated extensively [11,14,15], the chemotactic behavior of bacteria in complex environments involving multiple chemical gradients is still unclear. The natural habitat environment of bacteria, such as the mammalian gut and aquatic environments, is always spatially heterogeneous due to the fine spatial structures or randomly distributed nutrient hot spots [16–20], where multiple chemoeffectors from the same or different nutrient hot spots can generate complex gradients. The latter situation presents a dilemma for bacterial cells as they need to process conflicting signals from opposite directions and decide where to migrate to. As illustrated in Fig. 1(a), in an environment with opposing gradients of two attractants sensed by the two most abundant chemoreceptors, Tar and Tsr, respectively, there naturally emerges four distinct chemotactic strategies for a population of bacterial cells, as shown in Figs. 1(b)–1(e).

It is natural to expect that these different behaviors depend on the relative abundance of Tar and Tsr, which was found to depend on the cell culture density by Salman and Libchaber [21]. Indeed, in an earlier work by Kalinin *et al.* [22], the authors studied *E. coli* chemotaxis behaviors in a microfluidic channel with fixed opposing gradients of MeAsp and serine, and showed that the chemotactic behaviors depend on the cell culture density [characterized by optical density (OD)] at which cells were collected. In most cases bacterial populations exhibited a "winner-take-all" behavior with cells migrating to

*Corresponding author: yuhai@us.ibm.com
†Corresponding author: pkuluocx@pku.edu.cn
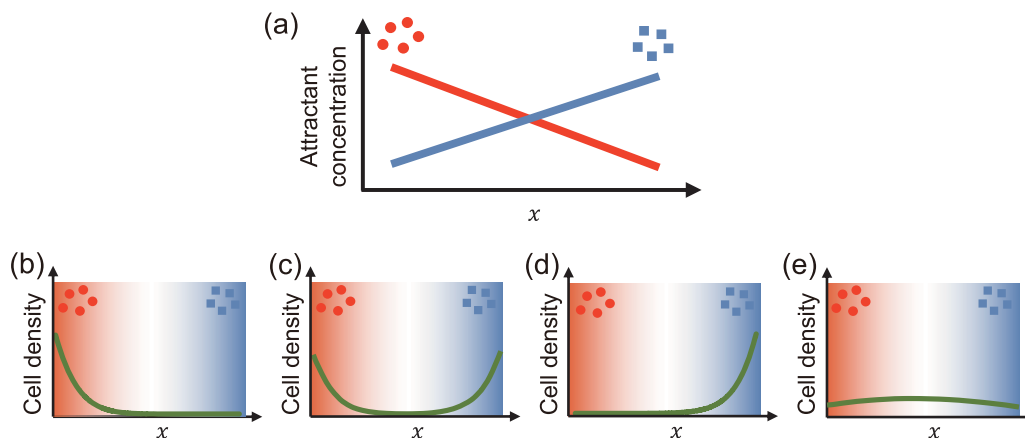
FIG. 1. Schemes of possible chemotactic strategies of the bacterial population in dual opposing gradients of attractants. (a) Schematic diagram of the opposing gradients of attractants. Two kinds of attractant molecules diffuse from the left (red) and right (blue) sides of the x axis, respectively. [(b)-(d)] Four different possible chemotactic behaviors for bacterial populations: unidirectional taxis to (b) the left end or (d) the right end, (c) bidirectional taxis to both ends, and (e) no taxis.

either the MeAsp side (high OD) or the serine side (low OD) of the channel depending on the relative abundance of Tar and Tsr, similar to those cases illustrated in Figs. 1(b) and 1(d). For a small regime of intermediate OD (or Tar/Tsr ratio) in the Kalinin *et al.* study [22], the population of *E. coli* did show a bimodal distribution similar to that illustrated in Fig. 1(c). However, it was not identified as a distinct population behavior possibly because the authors regarded it as the result of boundary effect.

Although the Kalinin *et al.* work studied the relationship between chemotactic preference and the average Tar/Tsr ratio in cells, the dependence of the population behavior on the relative strength of the two competing gradients and the cell-to-cell variability of the Tar/Tsr ratio within a population are not well understood. Phenotypic heterogeneity is ubiquitous in all biological systems [23–25], and nongenetic phenotypic diversity is known to play an important role in chemotaxis of the bacterial populations [26,27]. The cell-to-cell variations in pathway gain [28], adaptation time [29], and tumble bias [30] all contribute to the heterogeneous chemotactic performance within a clonal bacterial population when climbing up a chemoattractant gradient. Diversity in chemotaxis helps to enrich bacterial functionalities in the population when climbing up a single attractant gradient [28,30,31]. Directly important to our work, Yoney and Salman reported that the relative abundance of chemoreceptors varies greatly among individual cells in a population collected at a given OD [32]. To elucidate the chemotactic behavior of bacteria in different environments with competing attractant stimuli, we investigated the chemotactic behavior of bacteria in opposing gradients of MeAsp and serine by varying their relative strength systematically in a microfluidic chip.

We found that the *E. coli* population exhibits all four different chemotactic behaviors (including the bimodal behavior) shown in Figs. 1(d) and 1(e), depending on the relative strength of the two attractant gradients. To understand the molecular mechanisms for the diverse behaviors, we used a population chemotaxis model based on intracellular signaling dynamics. Besides reproducing the experimental results

quantitatively, the model showed that the phenotypic diversity in the relative abundance of the chemoreceptors Tar and Tsr is crucial in enabling the different population behaviors. The predicted dependence of the population chemotactic behaviors on the Tar/Tsr ratio from our model was verified quantitatively by additional experiments with cells collected at different ODs.

II. RESULTS

A. Four different population chemotaxis behaviors in opposing gradients of MeAsp and serine

Various opposite linear gradients of MeAsp and serine were constructed in the observation channel of the microfluidic chip, as shown in Fig. 2(a) (see also Fig. S1 in the Supplemental Material [33]). Both attractant gradients decrease approximately from 2/3 of the loading concentration (near end to the source) to 1/3 of that (farther end from the source) in the observation channel. For convenience, the loading concentration of MeAsp in reservoir I, C_{MA}, was set at 2 mM, and the serine concentration in reservoir II, C_{ser}, was varied over three orders of magnitude in a series of parallel channels. We found four distinct population behaviors based on the distribution of bacteria in different attractant environments [Fig. 2(b)]: (i) MeAsp-taxis behavior (S1), where cells accumulate near the MeAsp end of the channel; (ii) dual-taxis behavior (S2), where cells accumulate at both ends of the channel, leading to a bimodal distribution; (iii) serine-taxis behavior (S3), where cells accumulate near the serine end of the channel; and (iv) no-(apparent-)taxis behavior (S4), where cells spread almost evenly in the observation channel and seemingly lose chemotaxis ability to either attractant.

For low serine gradients, the MeAsp gradient dominates, resulting in the S1-type behavior. As the serine gradient increases, it starts to dominate and the system exhibits the S3-type behavior. However, an excessive level of serine leads to a relapse of the MeAsp-taxis (S1-type) behavior due to the saturation of binding of serine to Tsr. The unidirectional
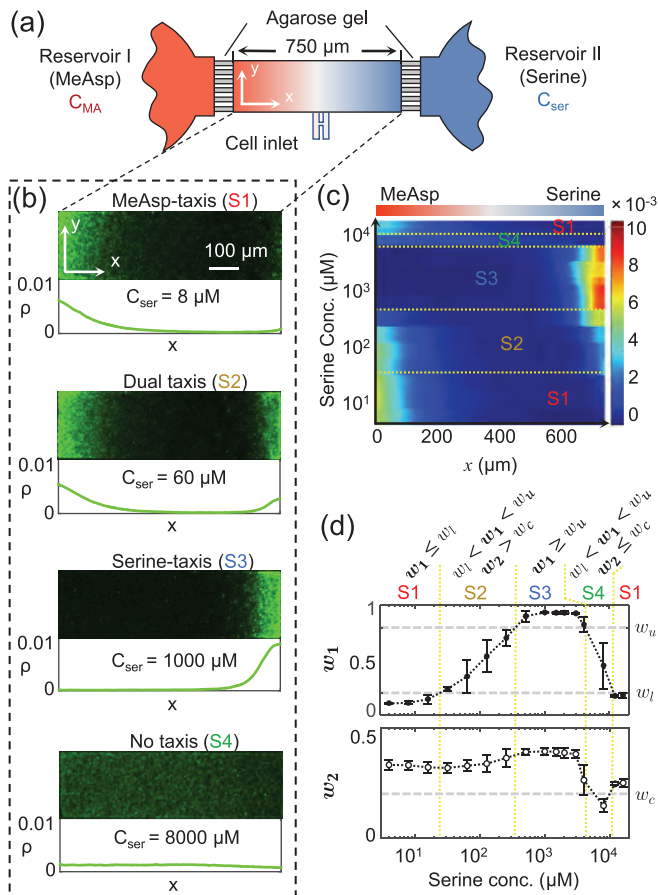
FIG. 2. Four kinds of chemotactic behaviors in a microfluidic channel with opposing attractant gradients. (a) Diagrammatic sketch of the microfluidic device. Reservoirs I and II contain MeAsp (red) and serine (blue), respectively. The MeAsp concentration is fixed at 2 mM while the serine concentration is varied between 4 μM and 16 mM. See the Supplemental Material [33] for details of the microfluidic chip architecture and fabrication. (b) Typical cell-density profiles of different chemotactic behaviors. Each one shows the real fluorescence photo (above) and the corresponding normalized cell-density profile averaged over the y direction (below). (c) The heat map displaying the cell density profiles for different serine concentrations. The whole map separates into five regions, and the corresponding chemotactic behavior types are labeled in each region. (d) The empirical criterion based on values of w_1 and w_2 (upper), and the corresponding changes of w_1 (middle) and w_2 (lower) in experiments shown in (c). The grey dashed lines show the threshold values ($w_l = 0.2$, $w_u = 0.8$, and $w_c = 0.2$) we used to distinguish the four different types of chemotaxis behaviors, which are divided by the yellow dotted lines in (c) and (d). Error bars indicate standard errors of three replicates.

taxis behaviors, S1 and S3, were reported in the previous study [22]. Two additional chemotactic behaviors, S2 and S4, were observed during the transition process as the system transitioned from S1 to S3 and back from S3 to S1. The heat map of cell density profiles under different attractant conditions indicates the S1-S2-S3-S4-S1 sequence of change in population behaviors as the serine concentration increases from 4 μM to 16 mM as shown in Fig. 2(c).

Two dimensionless chemotaxis parameters w_1 and w_2 were used to quantify the differences in chemotactic behavior based on the shape of cell density distribution in the channel: $w_1 = \bar{x}/L$ and $w_2 = \overline{|x/L - 1/2|}$, where the overbar denotes the mean value and x is the bacterial location. w_1 is the normalized average position of the cells, and w_2 is the normalized average distance of cells to the center of the channel, which characterizes the spread of the cell population. The S1-type behavior is characterized by a smaller value of $w_1 \leqslant w_l$, while the S3-type behavior has a large value of $w_1 \geqslant w_u$, where w_l and w_u are the lower and upper thresholds, which are set to be $w_l = 0.2$ and $w_u = 0.8$ in this paper. Both S2 and S4 behaviors have intermediate values of w_1, $w_l < w_1 < w_u$ [top panel of Fig. 2(d)]; however, they can be distinguished by their different values of w_2: S2-type behavior has a larger value of $w_2 > w_c$ while S4-type behavior has a smaller value of $w_2 \leqslant w_c$ [bottom panel in Fig. 2(d)], where w_c is a threshold value set to be 0.2 in this paper. By comparing the w_1 and w_2 values to their empirically determined threshold values, we classified the bacterial distributions into four types of chemotactic behaviors (w criterion).

B. Molecular mechanism for the four types of population behaviors

To understand the molecular mechanism responsible for the different population behaviors of bacteria in complex attractant environments with multiple opposing gradients, we used a population model of *E. coli* chemotaxis that is based on the dynamics of intracellular signaling pathways [34–37]. Importantly, relevant molecular details such as specific ligand-receptor binding (Tsr to serine and Tar to MeAsp) and the Tar/Tsr receptor ratio are included explicitly in the pathway-based population model, which allows us to test the hypothesis about the molecular origins of the observed behaviors and to make predictions that can be checked in experiments to test the hypothesis (see the Supplemental Material [33] for details of the pathway-based population model).

In environments with a single chemical gradient, simulations of the pathway-based population model with a fixed average chemoreceptor abundance worked well to capture the population behaviors of *E. coli* chemotaxis [38–40]. However, in the case of opposing gradients of MeAsp and serine, our initial simulations of the population behaviors using a fixed Tar/Tsr ratio for all cells missed the occurrence of the S2-type behavior, a key feature of our experimental results (Fig. S2 [33]). This prompted us to consider the effects of cell-to-cell variability in the Tar/Tsr ratio, which was shown to vary significantly in a genetically homogeneous population of cells [32]. For each individual cell in the population, we randomly assign a Tar/Tsr ratio (denoted by r) according to a log-normal distribution: $\log_{10} r \sim \mathcal{N}(\mu, \sigma)$. By proper choice of the mean (μ_0) and standard deviation (σ_0) that are consistent with experiments [32] as shown in Fig. 3(a), our model can quantitatively reproduce the main features of our experimental results, particularly the correct behavior sequence (S1-S2-S3-S4-S1) as the serine concentration (C_{ser}) increases [Figs. 3(b) and S2(b)]. The dependence of the two order parameters, w_1 and w_2, on C_{ser} is shown in Fig. 3(c), which shows a narrow range of S4-type behavior around $C_{ser} = 8000$ μM. Other
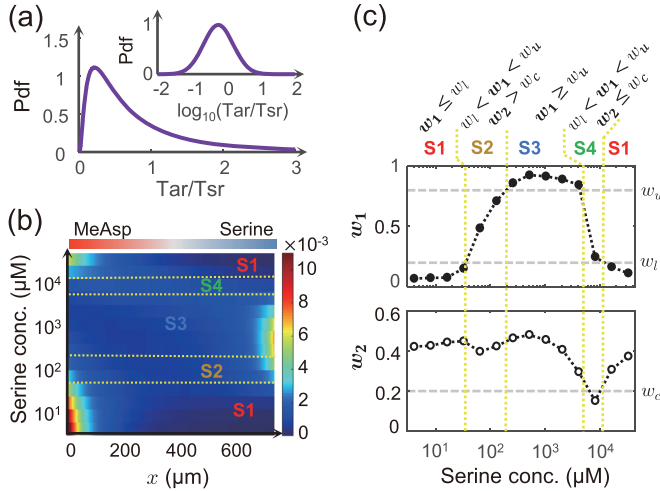
FIG. 3. Results from pathway-based population model. (a) The probability density function (Pdf) of the Tar/Tsr ratio (r) follows a log-normal distribution: $\log_{10}(r) \sim \mathcal{N}(\mu, \sigma)$. Inset: The normal distribution for $\log_{10}(r)$. $\mu = \mu_0 = -0.23$ and $\sigma = \sigma_0 = 0.43$ are used in our simulations here. (b) The heat map from simulations for different values of serine concentration in reservoir II ranging from 4 μM to 16 mM. Different types of chemotactic behaviors are separated by yellow dotted lines. (c) The corresponding chemotaxis order parameters w_1 and w_2 for different concentrations of serine. The four chemotactic behaviors were determined based on values of w_1 and w_2 as described in the text. Refer to Table S1 in the Supplemental Material [33] (see also Refs. [41–45] therein) to find the values of parameters used in simulation.

cell-to-cell variations such as cluster size and tumble bias can affect the response sensitivity to ligands or the drift velocity in attractant gradients significantly [28–30,46,47]. However, their effect on population behaviors in opposing attractant gradients is much less than that from cell-to-cell variability in the Tar/Tsr ratio (Figs. S3 and S4). Overall, the model results summarized in Fig. 3 are in quantitative agreement with our experiments shown in Fig. 2.

Due to its random run-and-tumble motion, the position of a cell with a fixed Tar/Tsr ratio r follows a probability distribution $\rho(x|r)$, which can be determined analytically from the pathway-based model with arbitrary serine and MeAsp gradients. As shown in Fig. 4(a) for the case of $C_{ser} = 60$ μM, cells accumulate near the serine or the MeAsp side for $r \leqslant 0.3$ or $r \geqslant 1$, respectively. For intermediate $0.3 < r < 1$, the balance of the two effectors results in a broad unimodal distribution that peaks in the middle of the channel. The cell distribution function with different r can be characterized by $x^*(r)$ defined as the position of maximum probability: $\frac{\partial \rho}{\partial x}\big|_{x=x^*} = 0$. The dependence of $x^*(r)$ on r as shown in Fig. 4(b) (bottom left) reveals a simple relationship between cell distribution and Tar/Tsr ratio: $x^*(r) = L$ for $r \leqslant r_1$ and $x^*(r) = 0$ for $r \geqslant r_2$, where r_1 and r_2 are the two critical Tar/Tsr ratios that depend on two competing attractant gradients [see the Supplemental Material [33], Eqs. (S20) and (S21)].

From our analysis above, the two unimodal population behaviors (S1 and S3) can be understood by comparing the population average Tar/Tsr ratio μ and the two gradient-dependent critical ratios r_1 and r_2. However, a large
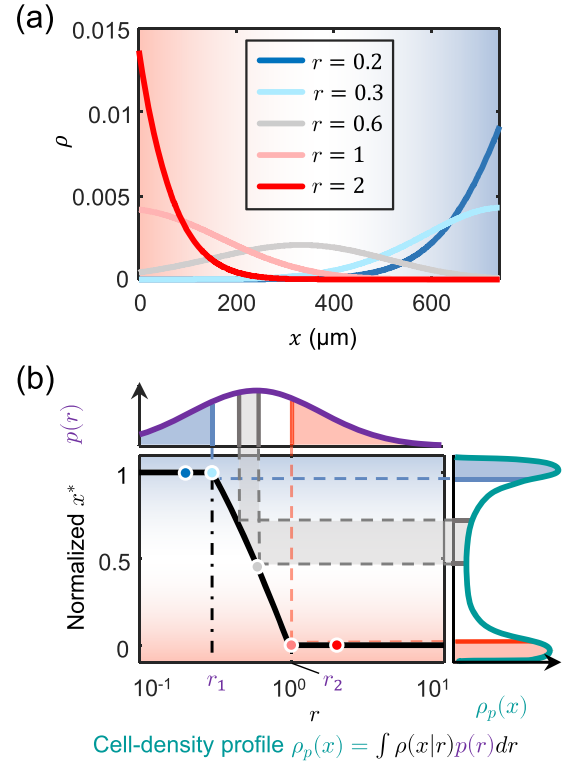
FIG. 4. Effects of the heterogeneity of the Tar/Tsr ratio in the population on population chemotactic behaviors. (a) Probability distribution of cells with different r for $C_{ser} = 60$ μM. (b) The normalized preferred location x^* versus r for $C_{ser} = 60$ μM (bottom). Colored dots on the r-x^* curve correspond to the cell probability distributions shown in (a) with the same color. Given a broad Tar/Tsr distribution $p(r)$ in the population (top), which overlaps with the two regions, $r \leqslant r_1$ and $r \geqslant r_2$, the corresponding population cell-density profile $\rho_p(x) = \int \rho(x|r)p(r)dr$ becomes bimodal; i.e., it exhibits S2-type behavior (right). The colors of shaded areas denote bacteria accumulating at the MeAsp side (light red), intermediate location (grey), and the serine side (light blue), respectively.

cell-to-cell variability in r as characterized by a large value of the standard deviation σ is essential for understanding the bimodal cell distribution, i.e., the S2-type behavior (Fig. S5). For a small σ, cells accumulate in the middle of the channel during the transition from S1 to S3. A bimodal cell distribution only appears for larger values of σ, and the range of S2-type behavior broadens as σ increases. For a broad Tar/Tsr ratio distribution $p(r)$ such as the one shown in Fig. 4(b) (top), which overlaps significantly with the two regions, $r \leqslant r_1$ and $r \geqslant r_2$, the corresponding population cell-density profile $\rho_p(x) = \int \rho(x|r)p(r)dr$ becomes bimodal; i.e., it exhibits the S2-type behavior as shown in Fig. 4(b) (right).

The S4-type behavior can be explained by sensing saturation for very high serine gradients. Specifically, for high serine gradients with $C_{ser} > 4000$ μM, we have $c_{min} \approx 1/3\ C_{ser} > K_{2a}$, with K_{2a} the dissociation constant of serine binding to Tsr; thus the Tsr receptors become saturated and less sensitive to the serine gradient. From the pathway-based population model, bacterial chemotaxis behaviors are controlled by an effective chemotaxis potential f_{total}, which consists of three independent parts: Tar-MeAsp sensing potential (f_1),

Tsr-serine sensing potential (f_2), and Tar-serine sensing potential (f_3), which is insignificant for controlling population behaviors. As C_{ser} increases, the gradient of f_2 along the channel becomes smaller due to the saturation effect, while the gradient of f_1 remains unchanged. As a result, the two gradients balance each other and the total effective potential f_{total} becomes roughly flat in the channel (with a shallow peak in the middle), which corresponds to the S4-type population behavior (see Fig. S6 [33]).

C. Phase diagram of chemotactic behaviors in different environments

As shown in Fig. 2, a given cell population exhibits different behaviors (distributions) depending on the relative strength of the two competing gradients. From our analysis in the last section, cells with $r \leqslant r_1$ have their locational probability peak at the serine end of the channel ($x = L$), while cells with $r \geqslant r_2$ have their locational probability peak at the MeAsp end ($x = 0$). Both r_1 and r_2 depend on the two gradients. In this study, we only vary the serine gradient, $c_{min} = c_{ser}(0) \approx \frac{1}{3}C_{ser}$, $c_{max} = c_{ser}(L) \approx \frac{2}{3}C_{ser}$, by changing the serine concentration C_{ser} in reservoir II, and the expressions for $r_{1,2}(c_{min}, c_{max})$ can be determined analytically from the pathway-based model. For a given population with a distribution $p(r)$ for the Tar/Tsr ratio r, the fraction of cells that accumulate near the serine side is given by $\Omega_1(c_{min}, c_{max}) \equiv \int_0^{r_1(c_{min}, c_{max})} p(r)\, dr$, and the fraction of cells that accumulate near the MeAsp side is given by $\Omega_2(c_{min}, c_{max}) \equiv \int_{r_2(c_{min}, c_{max})}^{\infty} p(r)\, dr$. Clearly, a large value of Ω_1 or Ω_2 indicates the cell population will accumulate near the serine or the MeAsp side, respectively. In the following, by comparing Ω_1 and Ω_2 with a threshold fraction Ω_c, we determine the phase diagram of the cell population behaviors in the ligand gradient space spanned by c_{min} and $\Delta c \equiv c_{max} - c_{min}$. First, the critical line $\Omega_1(c_{min}, c_{max}) = \Omega_c$ determines two regions in the ligand (environment) space ($c_{min}, \Delta c$), one of which corresponds to the environment conditions where a large portion of the cells have their maximum probability peak at the serine side (PSS). Similarly, the critical line $\Omega_2(c_{min}, c_{max}) = \Omega_c$ determines two other regions in the environment space ($c_{min}, \Delta c$), one of which corresponds to the environment conditions where a large portion of the cells have their maximum probability peak at the MeAsp side (PMS). These two critical lines naturally divide the phase diagram into four regimes (I–IV), as shown in Fig. 5(a) with regime I, $\Omega_1 < \Omega_c, \Omega_2 > \Omega_c$; regime II, $\Omega_1 > \Omega_c, \Omega_2 > \Omega_c$; regime III, $\Omega_1 > \Omega_c, \Omega_2 < \Omega_c$; and regime IV, $\Omega_1 < \Omega_c, \Omega_2 < \Omega_c$. Note that since Ω_1 and Ω_2 depend on c_{max} and c_{min} continuously (smoothly), the choice of Ω_c value does not cause sharp changes in the two critical lines (Fig. S7 [33]). In particular, the phase diagram by setting $\Omega_c = 0.12$ is consistent with the simulation results [Fig. 5(b)] where each cell-density profile from simulation is assigned to one of the four population behavior states according to the w criterion as described in the previous section. So, it confirms that regimes I–IV in the phase diagram correspond to the four chemotactic behaviors, respectively, and the Ω criterion is equivalent to the w criterion. In the experimental setup for results shown in Fig. 2(d), we have $c_{max} \approx 2c_{min}$, which corresponds to the diagonal line shown in the phase diagram
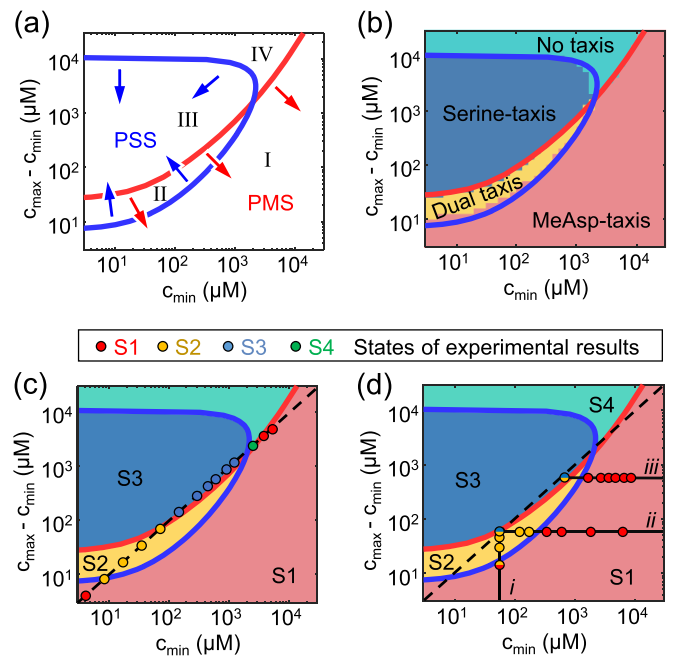
FIG. 5. The phase diagram for four chemotactic population behaviors and experimental verification. (a) The two critical lines $\Omega_1(c_{min}, c_{max}) = \Omega_c$ (blue line) and $\Omega_2(c_{min}, c_{max}) = \Omega_c$ (red line) separate the phase space into four regimes. The red arrows indicate the regime with $\Omega_2 > \Omega_c$, the PMS regime, and the blue arrows point to the PSS regime with $\Omega_1 > \Omega_c$. $\Omega_c = 0.12$ is used. (b) The population behaviors (S1, S2, S3, and S4) from simulations of the pathway-based population models based on the w criterion [see Fig. 2(d)] are shown as different colors, which are consistent with the phase diagram in (a). [(c) and (d)] Verifications of the phase diagram with (c) experimental results in Fig. 2 and (d) another three sets of experiments by fixing (i) $c_{min} = 67$ μM, (ii) $c_{max} - c_{min} = 67$ μM, and (iii) $c_{max} - c_{min} = 667$ μM, respectively. Each dot in (d) represents two repeats of experiments for a different choice of c_{min} and c_{max}. The colors of the dots represent the population behavior state (S1–S4). The dots with half yellow and half blue (or red) showed either S2 or S3 (or S1) in different experiments.

[Fig. 5(c)]. The experimentally observed population behaviors as shown by the colors of the dots in Fig. 5(c) are in agreement with those predicted from the phase diagram with $\Omega_c = 0.12$. The detailed form of the $p(r)$ distribution used in the simulations does not change the phase diagram significantly as long as they have the same mean and standard deviation; e.g., the phase diagram obtained using a gamma distribution for $p(r)$ is also in good agreement with the experimental results (Fig. S8).

Besides the initial set of experiments shown in Fig. 2 with $c_{max} - c_{min} \approx c_{min}$, to further test the phase diagram obtained from the population model, we measured the population behaviors in three additional sets of experiments (Fig. S9): (i) $c_{min} = 67$ μM, (ii) $c_{max} - c_{min} = 67$ μM, and (iii) $c_{max} - c_{min} = 667$ μM, which are shown in Fig. 5(d), where each dot represents an individual experiment. As shown in Fig. 5(d), the population behavior determined based on the w criterion shown as the different colors of the dots is consistent with that predicted from the phase diagram. The three dots, half yellow and half blue or red, indicate conditions that showed different
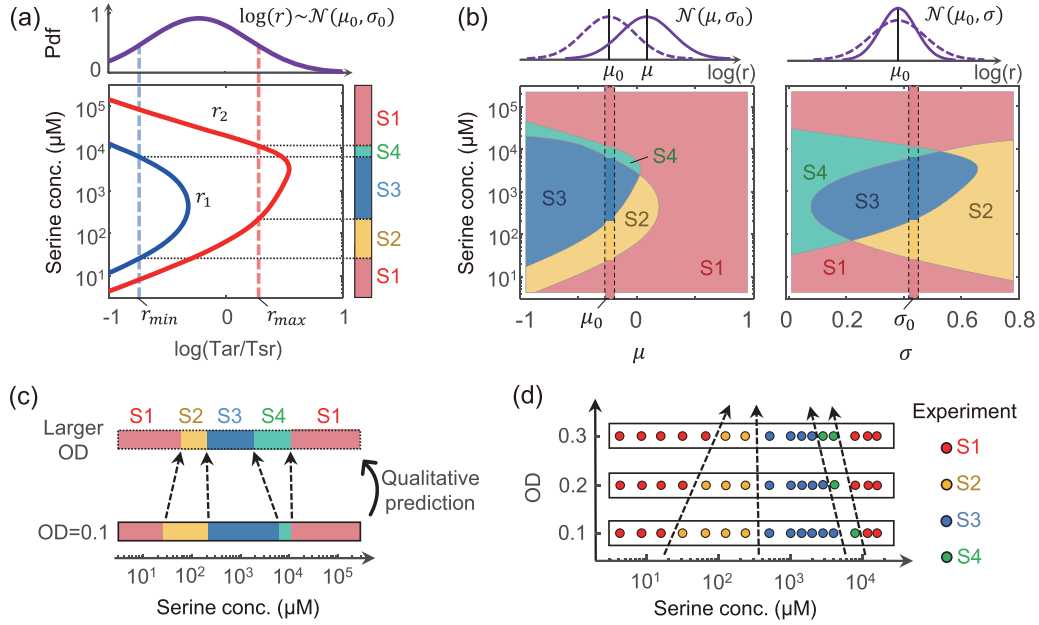
FIG. 6. Effect of Tar/Tsr distribution on the population chemotactic behavior. (a) Determining the chemotactic states (S1–S4) by comparing r_1 with $r_{\min}$, and r_2 with $r_{\max}$. (b) Changes in the span of each chemotactic behavior state with different values of parameters μ (left) and σ (right). The dotted box shows the simulation result with values of $\mu = \mu_0$ and $\sigma = \sigma_0$ used in the previous sections of our paper. (c) Model prediction for the changing trend of the spans of each population behavior state versus bacterial growth density (OD) based on the tendency of Tar/Tsr distribution with OD measured by Yoney and Salman [32]. (d) Experimental validation of the qualitative predictions in (c) with cell populations of different ODs. Each dot represents one experiment with a different C_{ser} and bacterial density.

behaviors (S2, or S3 or S1) in different experiments, which are consistent with the fact that the serine concentrations in these experiments (dots) are close to the (blue) critical lines.

A chemoreceptor can sense ligands other than its cognate attractant; e.g., Tar can bind serine albeit with a much lower affinity [48,49]. Though we incorporate the term of Tar-serine sensing, f_3, in all our model simulations and analysis, we claim that it does not change the qualitative conclusions. Quantitatively, by comparing the simulation results with and without including Tar-serine sensing (Fig. S10), we show that it only affects bacterial behaviors around C_{ser} of $10^3 \sim 10^4$ μM by enlarging the value of r_2 several times [Fig. S10(a) and S10(b)], which promotes the emergence of S4-type behavior. For example, a larger r_2 at $C_{\mathrm{ser}} = 8000$ μM shown in Fig. S10(c) means that less cells will migrate towards the MeAsp side and as a result the population behavior chnages from S1 type to S4 type [Fig. S10(d)]. Figures S10(e) and S10(f) show a subtle difference between the phase diagrams though: they indicate that the Tar-serine sensing expands the S4 regime, which makes the S4-type behavior observable in our experiments.

Based on the phase diagram, further analysis of the S4-type behavior shows that the ranges between r_1 and r_2 became broader as $\Delta c (= c_{\max} - c_{\min})$ increases [Fig. S11(a)]. We can predict from the simulation results that, under some environment conditions within the S4-type behavior, the cell density profile could form a peak near the middle of the channel [Fig. S11(b)], instead of spreading evenly across the channel. However, our current microfluidic chip design limits the experimental conditions to be below the diagonal of the phase diagram outside the regime of the appearance of the S4

peak. Improvement of the chip design is needed to verify the prediction.

D. OD-dependent Tar/Tsr ratio distribution modulates the population chemotactic behaviors

In the previous sections, we studied the population chemotactic behaviors of a population of cells with a given distribution $p(r)$ of the Tar/Tsr ratio r. In this section, we investigate how the population behavior changes as a function of $p(r)$, which typically follows a log-normal distribution: $\log_{10}(r) \sim \mathcal{N}(\mu, \sigma)$. The question we try to address is how the population behavior depends on the mean μ and the variance σ^2. To understand this question, we define two critical Tar/Tsr ratios $r_{\min}$ and $r_{\max}$ determined by $\int_0^{r_{\min}} p(r) \, dr = \Omega_c$ and $\int_{r_{\max}}^{\infty} p(r) \, dr = \Omega_c$, where Ω_c is the critical fraction introduced in the previous section. It is clear that both $r_{\min}$ and $r_{\max}$ depend on μ and σ^2. The two critical lines introduced in the last section (the blue and red lines in Fig. 5) are given by $r_1(c_{\min}, c_{\max}) = r_{\min}(\mu, \sigma)$ and $r_2(c_{\min}, c_{\max}) = r_{\max}(\mu, \sigma)$. As shown in Fig. 6(a), for the case with $c_{\max} - c_{\min} = c_{\min}$, the comparison of r_1 and $r_{\min}$ and that of r_2 and $r_{\max}$ together determine the range of the four chemotactic behaviors. Therefore, changing $p(r)$ alters the values of $r_{\min}$ and $r_{\max}$, which ultimately affects the span range of each state [Fig. 6(b)]. Specifically, since μ denotes the mean relative abundance of Tar/Tsr, changes in μ mainly affect the spans of the two unidirectional-taxis states S1 and S3 while the S2 and S4 states only exist in a narrow range in C_{ser} for medium to low values of μ [Fig. 6(b), left]. On the other hand, changing the variance σ^2 strongly affects the S2 and S4 states with

a smaller or larger σ^2 favoring the S4 or the S2 behavior, respectively [Fig. 6(b), right]. The relative expression level of Tar has been reported to increase at higher ODs [22,32], presumably to meet the increased demand for amino acids sensed by Tar [49]. The Tar/Tsr ratio in *E. coli* populations at different growth densities measured by Yoney and Salman [32] approximately follows a log-normal distribution with the mean μ increasing and standard deviation σ decreasing as OD increases (Fig. S12). Though a different culture medium was used in our experiments, the OD-dependent Tar/Tsr distribution provides a chance to experimentally validate the model predictions. Specifically, by referring to the experimentally measured change tendency of μ and σ with OD, our model qualitatively predicts that, as OD increases, the spans of S2 and S3 narrow until their disappearance while the regimes of S1 and S4 widen [Fig. 6(c)].

To validate these predictions, we performed experiments in the same chemotactic environments as in Fig. 2 but using two other *E. coli* populations collected at OD = 0.2 and 0.3 (Fig. S13; cells with OD = 0.1 were used in experiments shown in Fig. 2). Experimental results for these *E. coli* populations at higher ODs showed the preserved sequential behavioral state change of S1-S2-S3-S4-S1 with increasing serine concentration (Fig. S13). The dependence of the spans of the four behavioral states on the OD of the *E. coli* population agrees with the model predictions [Fig. 6(d)].

III. DISCUSSION

In realistic environments, there can be multiple and competing chemoeffectors that guide the chemotactic motion of the cells. In this paper, we systematically studied the population-level chemotaxis behaviors for *E. coli* cells in a microfluidic channel with opposing gradients of two attractants—serine and MeAsp—by fixing the MeAsp gradient and varying the opposing gradient of serine. Our experiments revealed four distinct population behaviors (S1–S4). When one of the chemical effectors is dominant (either with a much higher chemotaxis efficacy or with a much higher abundance of the corresponding chemoreceptor), the bacterial population migrates towards the dominant chemical effector and the cell density profile peaks near the maximum of the dominant chemoeffector, which is consistent with previous studies [22]. As the concentration of serine increases from a few micromoles to tens of millimoles, the influence of serine on bacterial behavior is initially small, then becomes progressively more dominant, attracting all bacteria to its side, but eventually serine loses its appeal due to saturation of the Tsr receptors. As a result, the *E. coli* population behavior goes from the MeAsp-dominant state (S1) to the serine-dominant state (S3) and back to S1 again as serine concentration increases. Moreover, we found two interesting chemotactic behaviors during the two transitions between the two unidirectional taxis states: a dual-taxis state (S2), in which the cell population density develops a bimodal distribution at the first transition from state S1 to state S3 ($C_{\text{ser}} \sim 10^2$ μM), and a no-taxis state (S4), in which the cell population density spreads broadly in the middle of the channel at the second transition from state S3 to state S1 ($C_{\text{ser}} \sim 10^4$ μM).

By combining microfluidic experiments and a quantitative population model that takes into account the dynamics of the intracellular chemotaxis signaling pathway, we showed that the mechanism of these different chemotactic behaviors is due to the interplay between the phenotypic variations of the relevant chemoreceptors and the competing attractant gradients. Though the relative abundance of Tar/Tsr is known to be important in thermotaxis and pH taxis, as well as chemotaxis under competing attractant gradients [22,32,50,51], the effect of the variability in the Tar/Tsr ratio on chemotaxis behaviors has not been fully explored. In comparison to the cell-to-cell variability in tumble bias and run speed, which can affect the cell population's search strategy and drift speed towards a single source of nutrient [28], our results showed that the cell-to-cell variability in the Tar/Tsr ratio [32,46] allows the cell population to make decisions on whether and how to partition the full population in search of different nutrient sources. For example, the cell-to-cell variation of the Tar/Tsr ratio is responsible for the dual-taxis behavior (S2), which enables the "betting on both sides" strategy to increase the population's fitness in fluctuating or uncertain environments [52–54]. Though the expression level of chemoreceptors varies across strains, culture mediums, and growth periods, our experimental and model results can still help study how chemotactic cells behave and benefit from complex environments when the distribution of receptors in the population is determined.

Bacterial chemotaxis is believed to evolve to adapt to complex environments and achieve optimal growth [55–58]. We believe that the collection of diverse population behaviors driven by the alternate dominance of different chemoreceptors and variability in the relative abundance of chemoreceptors may play a critical (enabling) role for maximizing population payoff. As serine concentration increases, an overall S1-S3-S1 sequence of change is easy to understand since a moderate level of serine can provide larger (potential) payoff than MeAsp while excess serine impairs bacterial growth. As for S2 and S4 during the two transitions between S1 and S3, a question arises: Why do bacteria hedge their bets in certain environments and spread evenly in others? Is it just a by-product of the heterogeneity of the relative abundance of chemoreceptors or is it an evolved strategy to optimize growth in changing environments? At the first transition from state S1 to state S3 where the serine concentration is relatively low, it may be risky for the entire population to migrate collectively from the MeAsp-rich side to the serine-rich side. In this case, a safer way to increase the overall payoff may be achieved by the S2-type behavior: the full population splits into two subpopulations, each of which centers around one end of the channel to take advantage of both attractants at the whole population level. However, when both attractants are abundant, the S4-type behavior is beneficial for the co-utilization of both nutrients. Further quantitative work (both experimental and modeling) is needed to explore the relation between the spatial distribution of cells as a result of chemotaxis in opposing attractant gradients and the possible population payoff in growth from cells utilizing different local nutrients, and to understand how the population benefits from the different relative abundance of chemoreceptors observed at different growth stages [32,51].

APPENDIX: METHODS AND MATERIALS

a. Cell strains, culture, and cell preparation. The *E. coli* strain used throughout this work is RP437 [59], a deviation from K12, wild-type *E. coli* commonly used for chemotaxis studies. They were transformed with a plasmid conferring ampicillin resistance and constitutively expressing green fluorescent protein (GFP) for visualization. *E. coli* cells were grown in tryptone broth (TB, 1% NaCl, 1% Bacto-Tryptone, pH 7.3) supplemented with 50 μg/ml ampicillin in a shaking bath at $32\,^\circ$C at 220 rpm. The culture grown overnight was diluted 1:50 (corresponding to an optical density at 600 nm of $OD_{600} \sim 0.01$) in fresh medium and grown in the shaker bath to $OD_{600} \sim 0.1$ or other ODs. The harvested cells were washed twice with chemotaxis buffer (CB, 10 mM phosphate buffer, 0.1 mM EDTA, 1 μM methionine, 10 mM lactic acid, pH 7.3). Cells were resuspended in CB and incubated at $32\,^\circ$C for 10 min to recover motility.

b. Data acquisition and imaging. Bacterial cells transferred with a plasmid expressing GFP were loaded into the cell-loading pool. The real-time cell density is estimated using the local image intensity of GFP. Shoots for each microchannel were taken automatically every 5 min for 5 h to record the fluorescence intensity across the observation channel using a Nikon Ti-E inverted microscope, $10\times$ objective lenses.

c. Data analysis. For each movie series, we averaged the fluorescence intensity of each frame along the *y* axis to obtain the cell density distribution along the attractant gradients at each time point. Then we calculated the average distribution for the period from 0.5 to 3 h. To know where cells peak, after smoothing and normalization for the spatial distributions, the high cell densities $\rho(x)$ (above the average value) were used to calculate w_1 and w_2 as described in the text and assigned to one of the four population behaviors according to the w criterion.

[1] N. Wadhwa and H. C. Berg, Bacterial motility: Machinery and mechanisms, Nat. Rev. Microbiol. **20**, 161 (2022).

[2] J. Wong-Ng, A. Celani, and M. Vergassola, Exploring the function of bacterial chemotaxis, Curr. Opin. Microbiol. **45**, 16 (2018).

[3] S. L. Porter, G. H. Wadhams, and J. P. Armitage, Signal processing in complex chemotaxis pathways, Nat. Rev. Microbiol. **9**, 153 (2011).

[4] M. A. Thomas, A. B. Kleist, and B. F. Volkman, Decoding the chemotactic signal, J. Leukocyte Biol. **104**, 359 (2018).

[5] G. H. Wadhams and J. P. Armitage, Making sense of it all: Bacterial chemotaxis, Nat. Rev. Mol. Cell Biol. **5**, 1024 (2004).

[6] G. L. Hazelbauer, J. J. Falke, and J. S. Parkinson, Bacterial chemoreceptors: High-performance signaling in networked arrays, Trends Biochem. Sci. **33**, 9 (2008).

[7] J. S. Parkinson, G. L. Hazelbauer, and J. J. Falke, Signaling and sensory adaptation in *Escherichia coli* chemoreceptors: 2015 update, Trends Microbiol. **23**, 257 (2015).

[8] G. H. Lan and Y. H. Tu, Information processing in bacteria: Memory, computation, and statistical physics: A key issues review, Rep. Prog. Phys. **79**, 052601 (2016).

[9] R. Colin and V. Sourjik, Emergent properties of bacterial chemotaxis pathway, Curr. Opin. Microbiol. **39**, 24 (2017).

[10] Z. W. Huang, X. Y. Pan, N. Xu, and M. L. Guo, Bacterial chemotaxis coupling protein: Structure, function and diversity, Microbiol. Res. **219**, 40 (2019).

[11] H. C. Berg and D. A. Brown, Chemotaxis in *Escherichia coli* analyzed by 3-dimensional tracking, Nature (London) **239**, 500 (1972).

[12] M. S. Li and G. L. Hazelbauer, Cellular stoichiometry of the components of the chemotaxis signaling complex, J. Bacteriol. **186**, 3687 (2004).

[13] D. Kentner and V. Sourjik, Spatial organization of the bacterial chemotaxis system, Curr. Opin. Microbiol. **9**, 619 (2006).

[14] S. Neumann, C. H. Hansen, N. S. Wingreen, and V. Sourjik, Differences in signalling by directly and indirectly binding ligands in bacterial chemotaxis, EMBO J. **29**, 3484 (2010).

[15] V. Sourjik and N. S. Wingreen, Responding to chemical gradients: Bacterial chemotaxis, Curr. Opin. Cell Biol. **24**, 262 (2012).

[16] Y. Wang, E. Holmes, E. M. Comelli, G. Fotopoulos, G. Dorta, H. Tang, M. J. Rantalainen, J. C. Lindon, I. E. Corthesy-Theulaz, L. B. Fay, S. Kochhar, and J. K. Nicholson, Topographical variation in metabolic signatures of human gastrointestinal biopsies revealed by high-resolution magic-angle spinning ^{1}H NMR spectroscopy, J. Proteome Res. **6**, 3944 (2007).

[17] C. Tropini, K. A. Earle, K. C. Huang, and J. L. Sonnenburg, The gut microbiome: Connecting spatial organization to function, Cell Host Microbe **21**, 433 (2017).

[18] R. N. Carmody, G. K. Gerber, J. M. Luevano, D. M. Gatti, L. Somes, K. L. Svenson, and P. J. Turnbaugh, Diet dominates host genotype in shaping the murine gut microbiota, Cell Host Microbe **17**, 72 (2015).

[19] G. P. Donaldson, S. M. Lee, and S. K. Mazmanian, Gut biogeography of the bacterial microbiota, Nat. Rev. Microbiol. **14**, 20 (2016).

[20] J. B. Raina, V. Fernandez, B. Lambert, R. Stocker, and J. R. Seymour, The role of microbial motility and chemotaxis in symbiosis, Nat. Rev. Microbiol. **17**, 284 (2019).

[21] H. Salman and A. Libchaber, A concentration-dependent switch in the bacterial response to temperature, Nat. Cell Biol. **9**, 1098 (2007).

[22] Y. Kalinin, S. Neumann, V. Sourjik, and M. Wu, Responses of *Escherichia coli* bacteria to two opposing chemoattractant

gradients depend on the chemoreceptor ratio, J. Bacteriol. **192**, 1796 (2010).

[23] B. M. C. Martins and J. O. W. Locke, Microbial individuality: How single-cell heterogeneity enables population level strategies, Curr. Opin. Microbiol. **24**, 104 (2015).

[24] D. Huh and J. Paulsson, Non-genetic heterogeneity from stochastic partitioning at cell division, Nat. Genet. **43**, 95 (2011).

[25] M. Ackermann, A functional perspective on phenotypic heterogeneity in microorganisms, Nat. Rev. Microbiol. **13**, 497 (2015).

[26] W. Yang and A. Briegel, Diversity of bacterial chemosensory arrays, Trends Microbiol. **28**, 68 (2020).

[27] J. P. Moore, K. Kamino, and T. Emonet, Non-genetic diversity in chemosensing and chemotactic behavior, Int. J. Mol. Sci. **22**, 6960 (2021).

[28] M. M. Salek, F. Carrara, V. Fernandez, J. S. Guasto, and R. Stocker, Bacterial chemotaxis in a microfluidic T-maze reveals strong phenotypic heterogeneity in chemotactic sensitivity, Nat. Commun. **10**, 1877 (2019).

[29] J. B. Masson, G. Voisinne, J. Wong-Ng, A. Celani, and M. Vergassola, Noninvasive inference of the molecular chemotactic response using bacterial trajectories, Proc. Natl. Acad. Sci. USA **109**, 1802 (2012).

[30] X. Fu, S. Kato, J. Long, H. H. Mattingly, C. He, D. C. Vural, S. W. Zucker, and T. Emonet, Spatial self-organization resolves conflicts between individuality and collective migration, Nat. Commun. **9**, 2177 (2018).

[31] J. Cremer, T. Honda, Y. Tang, J. Wong-Ng, M. Vergassola, and T. Hwa, Chemotaxis as a navigation strategy to boost range expansion, Nature (London) **575**, 658 (2019).

[32] A. Yoney and H. Salman, Precision and variability in bacterial temperature sensing, Biophys. J. **108**, 2427 (2015).

[33] See Supplemental Material at http://link.aps.org/supplemental/10.1103/PRXLife.2.013001 for details of the microfluidic chip architecture and fabrication, the attractant gradients used in simulations, the pathway-based population model, and theoretical derivation of the the phase diagram, which includes Refs. [38–41].

[34] X. Zhu, G. Si, N. Deng, Q. Ouyang, T. Wu, Z. He, L. Jiang, C. Luo, and Y. Tu, Frequency-dependent *Escherichia coli* chemotaxis behavior, Phys. Rev. Lett. **108**, 128101 (2012).

[35] Z. Li, Q. Cai, X. Zhang, G. Si, Q. Ouyang, C. Luo, and Y. Tu, Barrier crossing in *Escherichia coli* chemotaxis, Phys. Rev. Lett. **118**, 098101 (2017).

[36] G. Si, T. Wu, Q. Ouyang, and Y. Tu, Pathway-based mean-field model for *Escherichia coli* chemotaxis, Phys. Rev. Lett. **109**, 048101 (2012).

[37] X. Zhang, G. Si, Y. Dong, K. Chen, Q. Ouyang, C. Luo, and Y. Tu, Escape band in *Escherichia coli* chemotaxis in opposing attractant and nutrient gradients, Proc. Natl. Acad. Sci. USA **116**, 2253 (2019).

[38] L. L. Jiang, O. Y. Qi, and Y. H. Tu, Quantitative modeling of *Escherichia coli* chemotactic motion in environments varying in space and time, PLoS Comput. Biol. **6**, e1000735 (2010).

[39] T. S. Shimizu, Y. Tu, and H. C. Berg, A modular gradient-sensing network for chemotaxis in *Escherichia coli* revealed by responses to time-varying stimuli, Mol. Syst. Biol. **6**, 382 (2010).

[40] A. J. Waite, N. W. Frankel, and T. Emonet, Behavioral variability and phenotypic diversity in bacterial chemotaxis, Annu. Rev. Biophys. **47**, 595 (2018).

[41] G. Si, W. Yang, S. Bi, C. Luo, and Q. Ouyang, A parallel diffusion-based microfluidic device for bacterial chemotaxis analysis, Lab Chip **12**, 1389 (2012).

[42] B. A. Mello and Y. H. Tu, Effects of adaptation in maintaining high sensitivity over a wide range of backgrounds for *Escherichia coli* chemotaxis, Biophys. J. **92**, 2329 (2007).

[43] V. Sourjik and H. C. Berg, Receptor sensitivity in bacterial chemotaxis, Proc. Natl. Acad. Sci. USA **99**, 123 (2002).

[44] R. G. Endres and N. S. Wingreen, Precise adaptation in bacterial chemotaxis through "assistance neighborhoods", Proc. Natl. Acad. Sci. USA **103**, 13040 (2006).

[45] M. N. Levit and J. B. Stock, Receptor methylation controls the magnitude of stimulus-response coupling in bacterial chemotaxis, J. Biol. Chem. **277**, 36760 (2002).

[46] J. M. Keegstra, K. Kamino, F. Anquez, M. D. Lazova, T. Emonet, and T. S. Shimizu, Phenotypic diversity and temporal variability in a bacterial signaling network revealed by single-cell fret, eLife **6**, e27455 (2017).

[47] K. Kamino, J. M. Keegstra, J. Long, T. Emonet, and T. S. Shimizu, Adaptive tuning of cell sensory diversity without changes in gene expression, Sci. Adv. **6**, eabc1087 (2020).

[48] R. Mesibov and J. Adler, Chemotaxis toward amino-acids in *Escherichia coli*, J. Bacteriol. **112**, 315 (1972).

[49] Y. L. Yang, A. M. Pollard, C. Hofler, G. Poschet, M. Wirtz, R. Hell, and V. Sourjik, Relation between chemotaxis and consumption of amino acids in bacteria, Mol. Microbiol. **96**, 1272 (2015).

[50] B. Hu and Y. H. Tu, Precision sensing by two opposing gradient sensors: How does *Escherichia coli* find its preferred pH level? Biophys. J. **105**, 276 (2013).

[51] Y. L. Yang and V. Sourjik, Opposite responses by different chemoreceptors set a tunable preference point in *Escherichia coli* pH taxis, Mol. Microbiol. **86**, 1482 (2012).

[52] A. J. Grimbergen, J. Siebring, A. Solopova, and O. P. Kuipers, Microbial bet-hedging: The power of being different, Curr. Opin. Microbiol. **25**, 67 (2015).

[53] S. F. Levy, Cellular heterogeneity: Benefits besides bet-hedging, Curr. Biol. **26**, R355 (2016).

[54] B. Cerulus, A. M. New, K. Pougach, and K. J. Verstrepen, Noise and epigenetic inheritance of single-cell division times influence population fitness, Curr. Biol. **26**, 1138 (2016).

[55] J. Adler and B. Templeton, Effect of environmental conditions on motility of *Escherichia coli*, J. Gen. Microbiol. **46**, 175 (1967).

[56] A. Celani and M. Vergassola, Bacterial strategies for chemotaxis response, Proc. Natl. Acad. Sci. USA **107**, 1391 (2010).

[57] D. Lopez-Farfan, J. Reyes-Darias, and T. Krell, The expression of many chemoreceptor genes depends on the cognate chemoeffector as well as on the growth medium and phase, Curr. Genet. **63**, 457 (2017).

[58] J. F. Staropoli and U. Alon, Computerized analysis of chemotaxis at different stages of bacterial growth, Biophys. J. **78**, 513 (2000).

[59] J. S. Parkinson and S. E. Houts, Isolation and behavior of *Escherichia coli* deletion mutants lacking chemotaxis functions, J. Bacteriol. **151**, 106 (1982).